Published in final edited form as:
J Control Release. 2014 April 28; 180: 51–59. doi:10.1016/j.jconrel.2014.02.005.

A diaCEST MRI approach for monitoring liposomal accumulation in tumors

Kannie W.Y. Chan[1,2,3,7,*], **Tao Yu**[3,4,*], **Yuan Qiao**[6], **Qiang Liu**[6], **Ming Yang**[3,4], **Himatkumar Patel**[3], **Guanshu Liu**[1,2], **Kenneth W. Kinzler**[6], **Bert Vogelstein**[6], **Jeff W.M. Bulte**[1,2,4,7], **Peter C.M. van Zijl**[1,2], **Justin Hanes**[3,4,5], **Shibin Zhou**[6], and **Michael T. McMahon**[1,2,3,**]

[1]Russell H. Morgan Department of Radiology and Radiological Sciences, Division of MR Research, The Johns Hopkins University School of Medicine, Baltimore, MD 21287, United States.

[2]F.M. Kirby Research Center for Functional Brain Imaging, Kennedy Krieger Institute, Baltimore, MD 21205, United States.

[3]Center for Nanomedicine, The Johns Hopkins University School of Medicine, Baltimore, MD 21287, United States.

[4]Department of Biomedical Engineering, The Johns Hopkins University School of Medicine, Baltimore, MD 21205, United States.

[5]Department of Ophthalmology, The Wilmer Eye Institute, The Johns Hopkins University School of Medicine, Baltimore, MD 21287, United States.

[6]The Ludwig Center and Howard Hughes Medical Institute at the Hopkins-Kimmel Comprehensive Cancer Center, Baltimore, MD 21287, United States.

[7]Cellular Imaging Section and Vascular Biology Program, Institute for Cell Engineering, The Johns Hopkins University School of Medicine, Baltimore, MD 21205, United States.

Abstract

Nanocarrier-based chemotherapy allows preferential delivery of therapeutics to tumors and has been found to improve the efficacy of cancer treatment. However, difficulties in tracking nanocarriers and evaluating their pharmacological fate in patients have limited judicious selection of patients to those who might most benefit from nanotherapeutics. To enable the monitoring of nanocarriers *in vivo*, we developed MRI-traceable diamagnetic Chemical Exchange Saturation Transfer (diaCEST) liposomes. The diaCEST liposomes were based on the clinical formulation of liposomal doxorubicin (i.e. DOXIL®) and were loaded with barbituric acid (BA), a small, organic, biocompatible diaCEST contrast agent. The optimized diaCEST liposomal formulation with a BA-

**Corresponding author: mtmcmaho@gmail.com.
*Authors contributed equally

Supplementary data of this article can be found online at

to-lipid ratio of 25% exhibited 30% contrast enhancement at B_1=4.7 μT *in vitro*. The contrast was stable, with ~ 80% of the initial CEST signal sustained over 8 hrs *in vitro*. We used the diaCEST liposomes to monitor the response to tumor necrosis factoralpha (TNF-α), an agent in clinical trials that increases vascular permeability and uptake of nanocarriers into tumors. After systemic administration of diaCEST liposomes to mice bearing CT26 tumors, we found an average diaCEST contrast at the BA frequency (5 ppm) of 0.4% at B_1=4.7 μT while if TNF-α was co-administered the contrast increased to 1.5%. This novel approach provides a non-radioactive, non-metallic, biocompatible, semi-quantitative and clinically translatable approach to evaluate the tumor targeting of stealth liposomes *in vivo*, which may enable personalized nanomedicine.

Keywords

CEST; MRI; liposomes; barbituric acid; doxorubicin; tumor necrosis factor

1. Introduction

Nanocarrier-based delivery systems are being increasingly used for treating cancer and improving the therapeutic index of chemotherapeutic agents [1–3]. Their use allows the optimization of biodistribution and pharmacokinetics of therapeutics with minimal disruption of the drug itself, and hence can reduce adverse effects on normal tissue while enhancing drug efficacy. Nanocarriers, of an appropriate size (e.g. ~ 50–200 nm) and surface coating (e.g. with polyethylene glycol [PEG]), circulate for prolonged periods and preferentially accumulate in tumors through the enhanced permeability and retention effect (EPR) [4–6]. However, the complexity of the tumor microenvironment, including its abnormal vasculature [7], slow and variable blood flow, and low extracellular pH [8, 9] can affect the accumulation, distribution and retention of nanocarriers in tumors [8], and complicates studies to measure these parameters. In fact, previous work has shown that the outcome of nanocarrier-based chemotherapy varies among patients [8]. Whether this is due to differences in tumor uptake and retention of the nanocarriers, differences in drug metabolism in the host or tumor, or resistance mechanisms within the tumor, is not known [8]. It is therefore important to develop improved methods to track nanocarriers *in vivo* after administration to patients, in particular, imaging the accumulation in tumors allows a more comprehensive evaluation of their delivery and distribution.

Combination treatments employing molecular factors, such as tumor necrosis factoralpha (TNF-α), have been developed to improve the delivery of nanotherapeutics during chemotherapy. TNF-α is a proinflammatory cytokine known to augment the permeability of tumor vasculature [6, 10–14]. The combination of TNF-α and chemotherapeutics, such as doxorubicin, can increase treatment potency through synergistic effects [10, 11, 14]. It has been demonstrated that co-administration of TNF-α and liposomal doxorubicin (i.e. DOXIL®), suppressed solid tumors in animal models more effectively than treatment with DOXIL® alone [12, 13]. This combined therapy has now advanced into a clinical trial (clinical trial number: NCT01490047) for solid tumors. A non-invasive method for tracking the delivery of the nanocarriers to tumors in patients will help identify those who are more likely to benefit from the treatment.

Magnetic resonance imaging (MRI), a clinical modality with excellent spatial resolution, has shown great potential as a non-invasive way to monitor the distribution of nanocarriers *in vivo* [15–19]. Diamagnetic chemical exchange saturation transfer (diaCEST) is a "switchable" contrast mechanism that enables the detection of relatively low concentrations of exchangeable protons (at millimolar levels) present on non-metallic contrast agents [20–24]. Another advantage of this contrast mechanism is that it allows discrimination of different types of diaCEST contrast agents through their specific frequencies of exchangeable protons, which allows "multi-color" diaCEST imaging [25]. The sensitivity for detecting liposomal contrast agents can be improved by increasing the local concentration of exchangeable protons via their loading into liposomes [26]. It is thus possible to extend CEST technology to the nanotechnology realm through integrating CEST contrast agents into nanocarriers [26–30].

Here, we designed diaCEST stealth liposomes and evaluated their accumulation in tumors *in vivo* via non-invasive MRI. DiaCEST liposomes are lipid based-nanocarriers loaded with diaCEST contrast agents. These have been shown to allow liposome detection at picomolar levels *in vitro* and "multi-color" imaging of lymphatic drainage *in vivo* [28], but have not heretofore been shown to be useful for imaging experimental tumors. To achieve diaCEST contrast, we selected barbituric acid (BA) as the contrast agent, which is a heterocyclic pyridiminetrione that exhibits excellent contrast at a frequency of 5 ppm away from water [24]. BA-loaded diaCEST liposomes were systemically administered to mice bearing subcutaneous CT26 colon tumors, and were used to confirm that TNF-α co-treatment increases liposome accumulation within tumors via MRI. These liposomes were developed based on the formulation of clinically used DOXIL® and thus hold potential for clinical translation. The imaging of diaCEST liposomes for patient pre-screening may help to determine the potential effectiveness of DOXIL® therapy in individual patients.

2. Materials and Methods

2.1. Liposome preparation

Egg phosphatidylcholine (EPC), soy phosphatidylcholine (SPC), hydrogenated soy phosphatidylcholine (HSPC), 1,2-dipalmitoyl-*sn*-glycero-3-phosphocholine (DPPC), 1,2-disteoroyl-*sn*-glycero-3-phosphatidylcholine (DSPC), and 1,2-distearoyl-*sn*glycerophosphoethanolamine poly(ethylene glycol)$_{2000}$ (DSPE-PEG-2000) were obtained from Avanti Polar Lipids, Inc. (Alabaster, AL). Cholesterol and barbituric acid were purchased from Sigma-Aldrich (St. Louis, MO). Liposomes were formed by the lipid film hydration method as described [28, 31]. In brief, 25 mg of lipid mixture dissolved in chloroform was dried, and the resultant thin film was hydrated using 1 ml BA at 20 mg/ml and pH 7.3 to form multilamellar vesicles. The mixture was then annealed at 55–65 °C according to the type of PCs, sonicated, and subsequently extruded through stacked polycarbonate filters. DOX at 2 mg/ml was remotely loaded via sonication after extrusion. Liposomes were then filtered through Sephadex G-50 gel columns (GE Healthcare Life Sciences, Pittsburg, PA) to remove unloaded compounds, and stored at 4°C prior to use. The size (z-average) and heterogeneity in size (polydispersity index, PDI) were measured in PBS

at room temperature by dynamic light scattering using a Nanosizer ZS90 (Malvern Instruments, Southborough, MA).

2.2. Characterization of liposomal content and retention *in vitro*

To characterize the content (i.e., agent:lipid ratio), diaCEST liposomes were first freeze-dried, and further suspended in 10% v/v Triton X-100 solution. The encapsulated agent was then extracted by vigorous agitation of the suspended liposomes using a water bath sonicator at 42°C over an hour. After centrifugation (21,000 xg, 10 min), the supernatant was collected and further diluted in PBS. Fifty μL of the diluent was injected into a Shimadzu high performance liquid chromatography (HPLC) system equipped with a c18 reverse phase column (5 μm, 4.6×250 mm, Varian Inc., Santa Clara, CA). BA was eluted using an gradient mobile phase within first 3 min, phase 1: water (100%), changing to phase 2, water:acetonitrile (80%:20%, v/v)] and detected at 255 nm using a UV detector. Similarly, DOX was eluted using an isocratic mobile phase [water:acetonitrile (35%:65%, v/v)] and detected at 480 nm. Standard samples at known concentrations were first processed and calibration curves were generated as the reference for concentration calculations. Data were analyzed using LCsolution software (Shimadzu Scientific Instruments, Columbia, MD). Drug:lipid ratio was defined as the weight ratio of encapsulated agents to the dried lipid components of the liposomes.

To characterize the retention of BA in the diaCEST liposomes and the associated stability of the liposomal CEST contrast, 3 mL of newly prepared liposomes were instilled into a dialysis cassette (20 k Molecular Weight Cut Off, or MWCO, Thermo Scientific, Waltham, MA) and incubated in 200 mL PBS at 37C. Dialysis was first performed to ensure all unloaded agents were eliminated. At pre-determined time intervals, 100 μl of liposome suspension was collected from the dialysate, followed by *in vitro* CEST imaging and HPLC measurement. For the latter, collected liposomes samples were further suspended in 10% v/v Triton X-100 solution and thoroughly agitated using a water bath sonicator at 42°C, followed by centrifugation (21,000 xg, 10min). Quantitative analysis of the retained agents was then performed using HPLC as described above.

2.3. Animal model

All experiments conducted with mice were performed in accordance with protocols approved by the Johns Hopkins University Institutional Animal Care and Use Committee (IACUC). CT26 (CRL-2638) murine colorectal adenocarcinoma cells were purchased from the American Type Culture Collection (ATCC) and grown in McCoy's 5A Medium (Invitrogen/Life Technologies, Carlsbad, CA) supplemented with 10% Fetal Bovine Serum (FBS, HyClone, Thermo Scientific, Waltham, MA) at 37°C with 5% CO_2. Five million CT26 cells were injected subcutaneously into the right flank of female BALB/c mice (6–8 weeks; Harlan, Indianapolis, IN; ~20 g in weight), and allowed to grow for ~10 days.

2.4. CEST imaging *in vitro*

All MRI images were acquired at 310 K using an 11.7T Bruker Avance system (Bruker Biosciences, Billerica, MA). The B_0 field was shimmed using the shimming toolbox in Paravision Version 5.1 (Bruker BioSpin MRI GmbH). A modified rapid acquisition with

relaxation enhancement (RARE) sequence including a saturation pulse was used to acquire saturation images at different irradiation frequencies, which were used to generate the z-spectrum. A slice thickness of 1 mm was used, and the typical imaging parameters were: TE=4.3 ms, RARE factor=16, matrix size 128×64 and number of averages (NA)=2. The field of view was typically 13×13×1 depending on the number of phantoms. Two sets of saturation images were acquired, first the frequency map images for mapping of the spatial distribution of B_0, and the second set for characterization of the CEST properties. The acquisition time per frequency point was 12 s for frequency maps (TR=1.5 s) and 48 s for CEST images (TR=6.0 s).

For the B_0 frequency maps, WAter Saturation Shift Referencing (WASSR) was employed [32]. We used a saturation pulse length (t_{sat}) of 500 ms, saturation field strength (B_1) of 0.5 μT (21.3 Hz) and a saturation frequency increment of 50 Hz (spectral resolution=0.1 ppm) for WASSR images. We kept the image readout identical between the frequency map images and CEST images. For CEST images, we used t_{sat} = 4 s, B_1= 4.7 μT (200 Hz), and a frequency increment of 0.2 ppm.

2.5. CEST imaging *in vivo*

Mice were anesthetized using isoflurane and positioned in a 11.7T horizontal bore Bruker Biospec scanner (Bruker Biosciences, Billerica, MA). They were imaged before and 6 hrs after simultaneous tail vein administration of 150 μl of diaCEST liposomes at ~100 nM (~4 mg/mL BA as determined by HPLC) and 200 μl of TNF-α at 5 μg/ml. Two other groups of mice were treated with a single imaging agent (diaCEST liposomes) or TNF-α at the same dosage as the combination treatment. CEST images were acquired through collection of two sets of saturation images, a WASSR [32] set for B_0 mapping and a CEST data set for characterizing contrast. For the WASSR images, the saturation parameters were t_{sat}=500 ms, B_1=0.5 μT, TR=1.5 sec with saturation offset incremented from −1 to +1 ppm with respect to water in 0.1 ppm steps, while for the CEST images, t_{sat}=3 sec, B_1=4.7 μT, TR=5 sec, with offset incremented from −6 to +6 ppm (0.2 ppm steps) with a fat suppression pulse. The acquisition parameters were: TR=5.0 sec, effective TE=21.6 ms, RARE factor=12. The CEST images were acquired 6 hrs after the liposome and/or TNF-α administration.

MR images were processed using custom-written Matlab scripts with the CEST contrast quantified by calculating the asymmetry in the magnetization transfer ratio (MTR_{asym}) using $MTR_{asym}=(S_{-\Delta\omega}-S_{+\Delta\omega})/S_0$ for NH protons at the frequency offset from water (Δω)=5ppm. S_0 is the signal of water without saturation, S with saturation and therefore frequency dependent.. The relative MTR_{asym} was calculated by subtracting the pre-contrast from that of the post-contrast value of the whole tumor.

2.6. Fluorescence imaging and histology

Fluorescence imaging was performed and analyzed with a Spectrum/CT IVIS® *in vivo* imaging system using Living Image® software (PerkinElmer, Waltham, MA) respectively. Fluorescence signal (emission=620 nm, excitation=570 nm) was quantified as radiant efficiency. Excised tumors were imaged immediately after MRI and processed for histology. Tumor sections of 5 μm were stained with 4',6-diamidino-2-phenylindole (DAPI) for nuclei

and examined under a inverted microscope (Olympus, Tokyo, Japan). Images shown in Fig. 5B are overlay images of blue and red channels, representing $DAPI^+$ nuclei and $rhodamine^+$ liposomes, respectively [33].

To illustrate the vasculature within the tumor tissues, additional tumor sections of 5 μm from similar regions as the fluorescence sections were immunostained for CD31. In brief, tissue sections were deparaffinized and rehydrated, and endogenous peroxidase activity was blocked by 10 min treatment with peroxidase blocking reagent (Dako, Carpinteria, CA). The primary antibody (rabbit polyclonal anti-CD31; Thermo-Fisher, Waltham, MA) was applied at a dilution of 1:50 in antibody dilution buffer (ChemMate, San Dimas, CA) and incubated 45 minutes at room temperature. The primary antibody was detected using the Power Vision Plus HRPpolymer detection system (Leica Microsystems, Buffalo Grove, IL) as per manufacturer's instructions. All washing steps utilized Tris Buffered Saline with Tween (TBST; Sigma-Aldrich, St. Louis, MO). DAB chromogen (Sigma-Aldrich, St. Louis, MO) was applied to develop the secondary detection reagent. Slides were then counter stained with Mayer's hematoxylin (Dako, Carpinteria, CA) and dehydrated.

2.7. Cytotoxicity Study

HEK293 and HepG2 cells were obtained from ATCC and were cultured in DMEM medium and MEM medium, respectively, supplemented with 10% fetal calf serum 1% penicillin/ streptomycin (Gibco). A cell survival assay was performed using the Cell-Counting Kit-8 (Dojindo Molecular Technologies, Rockville, MD). Cells were seeded in 96-well plates at 10^4 cells per well, and incubated at 37°C with 5% CO_2. Then, BA at predetermined concentrations in culture medium, i.e., 10, 5, 1, 0.1, 0.01 and 0.001 mg/ml and control without BA, were added respectively and incubated for 24 hrs before the survival assay. For the assay, cells were incubated in medium with 10% CCK-8 solution for an hour. The absorbance of each well was then measured at 450 nm with a plate reader (Synergy Mx microplate reader, BioTek, Winooski, VT). Cell survival was quantified as the absorbance normalized by the control values.

2.8. Statistical Analysis

Statistical analysis was performed on the relative MTR_{asym} values and the fluorescence measurements of the liposomes group (n=5), the liposomes+TNF-α group (n=5), and the TNF-α group (n=3) using one-way analyses of variance (ANOVA) followed by post-hoc tests.

3. Results

3.1. Properties of BA

We designed a diaCEST liposome for the MRI monitoring of augmented delivery of stealth liposomes after tumor vascular therapy using TNF-α (Fig. 1). We first investigated the diaCEST properties of BA as a function of concentration and pH to determine the optimal loading conditions for our liposomes (Fig. 2). At pH 7.4, the contrast of BA, as quantified by the magnetization transfer ratio asymmetry ($MTR_{asym}=(S_{-\Delta\omega}-S_{+\Delta\omega})/S_0$) at 5 ppm from the water frequency, increased linearly with concentrations up to about 10–20 mM (Fig. 2A).

The lowest concentration of BA measured was 1 mM with a contrast of ~2%. The pH dependence of the BA CEST effect is shown in Fig. 2B, with maximum contrast achieved at pH values around 7.3–8.0, and reduced contrast in more acidic environment, namely a decrease in MTR_{asym} of 4% from pH 7.5 to 7.0, and 15% from 7.5 to 6.5. This sensitivity can be explained by a base catalyzed proton exchange with water. The proton exchange rate on BA was measured to be ~0.9 kHz at pH 7.3–8.0 through QUESP analysis [34], with the reduction in contrast below this pH presumably due to a drop in exchange rate. At a pH value of ~ 9.0 and higher, there were changes in the frequency of maximum contrast in Fig. 2B, which are attributed to a deprotonation of the nitrogen on the heterocyclic ring from keto-enol tautomerism. This equilibrium is displayed in Fig. 2C.

3.2. Preparation of diaCEST liposomes

We next screened different formulations of diaCEST liposomes (Fig. 1) to optimize the composition for *in vivo* imaging. BA was the major cargo, with a low concentration of doxorubicin (DOX) co-loaded to mimic the DOXIL® formulation and investigate whether DOX co-loading affects liposomal diaCEST contrast. We also incorporated a trace amount of rhodamine-labeled lipids to enable fluorescence detection in tumors in order to validate our MRI findings (Fig. 1). Five liposomal formulations based on DOXIL® were tested with the same phosphatidylcholine (PC):cholesterol:PEGylated-lipid molar ratio of 59:38:3 mol %, but different types of PC (i.e. Egg PC, Soy PC, Hydrogenated Soy PC/HSPC, 1,2-dipalmitoyl-*sn*-glycero-3-PC/DPPC, and 1,2-distearoyl-*sn*-glycero-3-PC/DSPC), and BA was loaded at pH ~7.5. Their characterization data are listed in Table 1 (n=3 per formulation). All formulations resulted in similar sizes (Z-ave) of ~150 nm, with a low polydispersity index (PDI) below or around 0.1, suggesting relatively uniform size distribution (Table 1). Liposome size and PDI showed minimal changes after a 24-hr incubation in PBS at 37°C, demonstrating their robust physical stability *in vitro*. We also measured the content of BA in the diaCEST liposomes using HPLC and their MRI contrast using *in vitro* CEST imaging. The diaCEST contrast generated by these formulations (Table 1 and supplementary Fig. S1) ranged from 19% to 30% at ~100 nM concentration of liposomes, and was correlated with the amount of BA loaded (measured as the BA:lipid ratio). Liposomes based on DSPC had both the strongest diaCEST contrast of 30% and the highest BA loading of 25% BA:lipid ratio and, therefore, were selected as the lead formulation (Table 1). We estimated that the local concentration of BA was ~10^5 molecules per liposome; this high local concentration is hard to achieve *in vivo* without loading BA into liposomes, which is favorable for CEST imaging.

3.3. Stability and release of diaCEST liposomes

We next determined how stable this diaCEST contrast might be under physiological conditions. As shown in Fig. 3A, BA-loaded DSPC liposomes were dialyzed against PBS at 37 °C, and the BA content as well as the diaCEST contrast of the liposomes at 5 ppm were then measured at specific time points using HPLC and MRI, respectively. HPLC measurements showed that there was a mild burst release of BA over the first 2–4 hrs. After this, the BA content remained relatively stable for 24 hrs at ~ 15 mM, with ~ 80% of the initial dose retained (Fig. 3B). In comparison, the diaCEST contrast of the liposomes decreased continuously over the entire course of the experiment, with ~ 80% of the initial

intensity retained at 8 hrs and only ~ 50% at 24 hrs. Since our CEST measurements were performed at constant temperature and pH, the proton exchange rate should be minimally affected. Thus, this discrepancy between BA retention and diaCEST contrast generated is more likely due to a reduced number of exchangeable protons, which might result from the precipitation of BA within the liposomes due to an influx of salts, or from BA molecules becoming embedded inside the phospholipid bilayer.

3.4. CEST imaging *in vivo*

We then tested whether the diaCEST liposomes could be detected *in vivo* via MRI and be used to evaluate the effects of TNF-α co-treatment. We performed CEST imaging on mice bearing subcutaneous CT26 tumors before and after intravenous (i.v.) injection of diaCEST liposomes and TNF-α (Liposomes+TNF-α group), diaCEST liposomes only (Liposomes group) or TNF-α only (TNF-α group). Tumor sizes were kept between 50 and 100 mm^3 to minimize variations in liposome uptake between mice due to differences in the vasculature that become progressively more heterogeneous as tumors grow (Supplementary Fig. S4). This tumor size range is also consistent with previous investigations employing liposomes for treatment of experimental cancer [35, 36]. The imaging scheme for this study is shown in Fig. 4A. Pre-treatment CEST images were acquired as background for baseline referencing. Post-treatment images were acquired 6 hrs after the initial administration to allow sufficient time for tumors to respond to TNF-α treatment and for diaCEST liposomes to accumulate in tumors (Fig. 3B). Representative CEST contrast images (MTR_{asym} maps at 5ppm) of mice before and after treatment are shown in Fig. 4B. The negative MTR_{asym} observed in the histogram is presumably due to asymmetric magnetization transfer (MT) [37, 38] from semi-solid protons found in tissues, or relay transfers from aliphatic protons on the negative side of the z-spectrum to water through Nuclear Overhauser Effects (NOEs) [39, 40]. As compared to the pre-treatment baseline images, the diaCEST contrast (at 5 ppm) for the Liposome group increased slightly and accumulated in particular regions in the tumors. A relatively high CEST contrast was found at the periphery of the tumor, implying a constrained distribution of diaCEST liposomes within the tumors. In contrast, the co-administration of liposomes and TNF-α significantly increased the diaCEST contrast at 5 ppm (Fig. 4B). This enhancement was not confined to the tumor rim, but was spread throughout the tumor volume. This remarkable improvement in the spatial distribution is further highlighted through histogram analysis, which shows a wider range of CEST contrast values for the Liposome group, and a relatively uniform distribution of contrast values for the Liposomes+TNF-α group (Fig. 4B). To quantify the differences among the three groups, we normalized the MTR_{asym} profiles by the baseline contrast of the pre-treatment images. As shown in Fig. 4C, both liposome treatment groups displayed a characteristic peak in the MTR_{asym} plots at 5 ppm which was specific to BA (Fig. 4C, green box), whereas the control group with administered TNF-α in the absence of liposomes displayed no contrast at this offset frequency, indicating the contrast was specific to the BA-loaded diaCEST liposomes. The average relative MTR_{asym} of the Liposomes+TNF-α group (1.53±0.14%) was significantly higher (n=5; **, $P<0.01$) than that of the Liposome group (0.41±0.19%) (Fig. 4D). No significant difference was found in the relative MTR_{asym} at 5 ppm among the three groups in the muscle (Fig. 4D), indicating that the increase of CEST contrast is specific for the enhanced accumulation of BA liposomes in tumors due to the TNF-α treatment.

3.5. Fluorescence imaging and histology

To validate the differences in uptake visualized by CEST MRI, we harvested the tumors after imaging, and quantified the amount of intratumoral liposomes through measurements of the fluorescence from the rhodamine incorporated into the lipid bilayers (Fig. 5A). In agreement with the differences observed in CEST imaging, tumors from the Liposomes +TNF-α group mice showed a consistently higher fluorescence signal than from the Liposome group (n=5, *, $P<0.05$), with the average fluorescence intensity almost doubled as quantified by radiant efficiency. The efficacy of the TNF-α co-treatment was further validated by the histology of the tumors from both treatment groups (Fig. 5B). Consistent with the diaCEST and fluorescence measurements, tumor tissue from the liposome group displayed a smaller amount of red fluorescence from diaCEST liposomes with a confined spatial distribution. By comparison, tumor tissue from the Liposomes+TNF-α group displayed an overall larger amount of red fluorescence, indicating more diaCEST liposomes were accumulated across the entire tissue section. Moreover, TNF-α treatment also resulted in more pronounced CD31 staining within the tumor tissue, suggesting alterations of the tumor vasculature which could be the histologic basis for the enhanced liposome accumulation (Fig. 5C, arrows). These results confirm our MRI measurements.

4. Discussion

BA has several properties that are well-suited for diaCEST MRI. First, the exchangeable protons resonate further from water (at 5 ppm in Fig. 2A) than hydroxyl (~ 1 ppm), amine (~ 1.8 ppm), or amide (~ 3.6 ppm) protons. This larger shift minimizes interference of the direct water saturation, thereby increasing sensitivity and avoiding overlap with tissue metabolites possessing other exchangeable protons, e.g. glucose, L-glutamate, creatine, and glycosaminoglycans [39, 41–47]. Second, the detection limit for liposomes loaded with BA is significantly lower than free BA (which displays 2% contrast at 1 mM) due to the high local concentration of exchangeable protons in liposomes achieved by the loading method we used (Fig. 1). Finally, BA is the parent compound of barbiturate drugs, which have been administered to patients for over a century as central nervous system depressants. The efficacy of these barbiturate drugs relies on their potentiating effect on the $GABA_A$ receptor [48]. Unlike the barbiturate drugs, BA lacks the two 5-substitutents on the pyrimidinetrione ring that are critical to binding to the $GABA_A$ receptor [48], and thus BA is not pharmacologically active. Cytotoxicity studies confirmed that BA did not affect the survival of human hepatocytes and kidney cells at concentrations similar to the initial dosage of the BA liposomes (Supplementary Fig. S3). Moreover, previous reports also showed that BA was better tolerated than barbiturate drugs in mice, with a median lethal dose ~3-fold higher (~505 mg/kg, injected intraperitoneally) than that of a common barbiturate drug, barbital (~178 mg/kg) [49, 50], suggesting its better biocompatibility and safety *in vivo*. Based on these favorable features, we designed the BA-loaded diaCEST liposomes with the characteristic contrast at 5 ppm, and by using liposome as the nanocarrier, a high local concentration of BA (in millimolar) can be achieved for *in vivo* imaging. We chose the DSPC lipid, which possesses longer alkyl chains, and a higher melting temperature than the other lipids tested; as a result, the liposome bilayers are expected to be more rigid than other lipids, which could lead to a higher degree of BA retention in liposomes. Meanwhile, we

confirmed that this enhanced rigidity DSPC liposomes only resulted in a mild decrease of the exchange rate (~0.5 kHz compared to ~0.7 kHz in EPC liposomes; Supplementary Figure S2), which should not compromise the CEST contrast.

Previous studies have shown that it is possible to detect liposomes using metal based agents [18, 51–53], including a targeted liposome study performed by Flament et al. [30] and a direct intratumoral injection study by Castelli et al. at 7T [15]. In the current study, we demonstrate for the first time that tumor uptake of CEST liposomes can be detected *in vivo* via non-invasive CEST MRI using a small non-metallic molecule, BA, instead of a lanthanide complex, and show that enhanced permeability of tumor vessels and consequent liposome accumulation after systemic administration can similarly be demonstrated. Moreover, the contrast indicated the spatial distribution of liposomes, especially after TNF-α treatment. The typical dosage of DOXIL® in patients in terms of lipid contents is ~400 mg/m^2 (equivalent to 50 mg/m^2 DOX). In the current study, the dosage of the diaCEST liposomes expressed as lipid content is ~350 mg/m^2 (equivalent to ~85 mg/m^2 or ~30 mg/kg BA in mice), suggesting our dosage is comparable to that of DOXIL® and is clinically relevant. These results have implications for future clinical trials of liposomes and other nanoparticles, allowing a noninvasive, non-radioactive monitoring of the delivery of these particles to tumors.

Further optimization of our diaCEST approach may be possible. First, the CEST contrast for BA is pH sensitive, which might result in a decrease in contrast if BA is released from the intraliposomal space (pH ~ 7.4) to the slightly acidic extravascular space in tumors, leading to an underestimation of the amount of liposomes delivered. Additionally, the proton exchange of intraliposomal water molecules with the bulk water molecules might also be affected by changes in the biological environment. Further optimization using alternative diaCEST agents which produce higher contrast could improve the quantification and robustness of our diaCEST approach. Second, while we have demonstrated that BA liposomes produce significant CEST contrast for *in vivo* imaging, alternative loading approaches [54] or switching to another small organic diaCEST agent might enable a higher DOX content for theranostic diaCEST liposomes. Third, we acquired and assessed only one imaging slice in this study. Since tumors are heterogeneous, it would be ideal to collect multiple slices. To keep our evaluation simple and robust, we chose a standard long continuous wave CEST imaging sequence which results in a long imaging time. Acquiring more slices is possible using advanced imaging sequences [55–59].

5. Conclusions

We developed liposomes that contain BA as a diaCEST contrast agent for *in vivo* MRI monitoring, and demonstrated that BA-loaded liposomes can be detected using CEST imaging at a 5 ppm offset from water, far enough to be readily differentiated from the 1–2 ppm CEST contrast present in endogenous metabolites. The lead BA-liposome formulation exhibited 30% CEST contrast and 25% BA content *in vitro*, both of which were well maintained with ~80% of the initial intensity/dose retained over 8 hrs of dialysis against PBS. In mice bearing subcutaneous CT 26 colon tumors, we were able to detect diaCEST liposomes using CEST MRI, with an average increase in CEST contrast of 0.8% at 6 hrs

after i.v. tail vein administration. Co-treatment with TNF-α enhanced the accumulation and distribution of liposomes in tumors, with an additional increase in the CEST contrast of 1.1% at 5 ppm (total average contrast 1.5%), and more importantly, with more uniform intratumoral dissemination. These observations were validated by *ex vivo* fluorescence imaging and histology. Both the clinical relevance of the diaCEST formulations (as derived from DOXIL®) and the biocompatibility of BA should facilitate clinical translation of these diaCEST liposomes into the clinic.

Supplementary Material

Refer to Web version on PubMed Central for supplementary material.

Acknowledgments

The authors sincerely thank Abraham Anonuevo for helping prepare liposomes, Clark Zhang for helping cytotoxicity studies, Alan Meeker and Jessica Hicks for immunohistochemical staining, Qingguo Xu for helpful discussions. This work was supported by The Virginia and D.K. Ludwig Fund for Cancer Research, and NIH grants R01EB015031, R01EB015032, U54CA151838, R01EB012590, and CA62924.

Abbreviations

MRI	magnetic resonance imaging
CEST	chemical exchange saturation transfer
BA	barbituric acid
DOX	doxorubicin
TNF-α	tumor necrosis factor-alpha
HPLC	high performance liquid chromatography

References

1. Peer D, Karp JM, Hong S, Farokhzad OC, Margalit R, Langer R. Nanocarriers as an emerging platform for cancer therapy. Nat Nanotechnol. 2007; 2:751–760. [PubMed: 18654426]
2. Kumar P, Gulbake A, Jain SK. Liposomes a vesicular nanocarrier: potential advancements in cancer chemotherapy. Crit Rev Ther Drug Carrier Syst. 2012; 29:355–419. [PubMed: 22876808]
3. Strijkers GJ, Kluza E, Van Tilborg GA, van der Schaft DW, Griffioen AW, Mulder WJ, Nicolay K. Paramagnetic and fluorescent liposomes for target-specific imaging and therapy of tumor angiogenesis. Angiogenesis. 2010; 13:161–173. [PubMed: 20390447]
4. Klibanov AL, Maruyama K, Torchilin VP, Huang L. Amphipathic polyethyleneglycols effectively prolong the circulation time of liposomes. FEBS Lett. 1990; 268:235–237. [PubMed: 2384160]
5. Allen TM, Hansen C, Martin F, Redemann C, Yau-Young A. Liposomes containing synthetic lipid derivatives of poly(ethylene glycol) show prolonged circulation half-lives in vivo. Biochim Biophys Acta. 1991; 1066:29–36. [PubMed: 2065067]
6. Prabhakar U, Blakey DC, Maeda H, Jain RK, Sevick-Muraca EM, Zamboni W, Farokhzad OC, Barry ST, Gabizon A, Grodzinski P. Challenges and key considerations of the enhanced permeability and retention effect (EPR) for nanomedicine drug delivery in oncology. Cancer Res. 2013
7. Garcia-Roman J, Zentella-Dehesa A. Vascular permeability changes involved in tumor metastasis. Cancer Lett. 2013; 335:259–269. [PubMed: 23499893]

8. Danhier F, Feron O, Preat V. To exploit the tumor microenvironment: Passive and active tumor targeting of nanocarriers for anti-cancer drug delivery. J Control Release. 2010; 148:135–146. [PubMed: 20797419]
9. Wojtkowiak JW, Verduzco D, Schramm KJ, Gillies RJ. Drug resistance and cellular adaptation to tumor acidic pH microenvironment. Mol Pharm. 2011; 8:2032–2038. [PubMed: 21981633]
10. van Horssen R, Ten Hagen TL, Eggermont AM. TNF-alpha in cancer treatment: molecular insights, antitumor effects, and clinical utility. Oncologist. 2006; 11:397–408. [PubMed: 16614236]
11. Ten Hagen TL, Van Der Veen AH, Nooijen PT, Van Tiel ST, Seynhaeve AL, Eggermont AM. Low-dose tumor necrosis factor-alpha augments antitumor activity of stealth liposomal doxorubicin (DOXIL) in soft tissue sarcoma-bearing rats. Int J Cancer. 2000; 87:829–837. [PubMed: 10956394]
12. Brouckaert P, Takahashi N, van Tiel ST, Hostens J, Eggermont AM, Seynhaeve AL, Fiers W, ten Hagen TL. Tumor necrosis factor-alpha augmented tumor response in B16BL6 melanoma-bearing mice treated with stealth liposomal doxorubicin (Doxil) correlates with altered Doxil pharmacokinetics. Int J Cancer. 2004; 109:442–448. [PubMed: 14961585]
13. Qiao Y, Huang X, Nimmagadda S, Bai R, Staedtke V, Foss CA, Cheong I, Holdhoff M, Kato Y, Pomper MG, Riggins GJ, Kinzler KW, Diaz LA Jr, Vogelstein B, Zhou S. A robust approach to enhance tumor-selective accumulation of nanoparticles. Oncotarget. 2011; 2:59–68. [PubMed: 21378416]
14. Hoving S, Seynhaeve AL, van Tiel ST, Eggermont AM, ten Hagen TL. Addition of low-dose tumor necrosis factor-alpha to systemic treatment with STEALTH liposomal doxorubicin (Doxil) improved anti-tumor activity in osteosarcoma-bearing rats. Anticancer Drugs. 2005; 16:667–674. [PubMed: 15930896]
15. Castelli DD, Terreno E, Cabella C, Chaabane L, Lanzardo S, Tei L, Visigalli M, Aime S. Evidence for in vivo macrophage mediated tumor uptake of paramagnetic/fluorescent liposomes. NMR Biomed. 2009; 22:1084–1092. [PubMed: 19569084]
16. Terreno E, Boffa C, Menchise V, Fedeli F, Carrera C, Castelli DD, Digilio G, Aime S. Gadolinium-doped LipoCEST agents: a potential novel class of dual 1H-MRI probes. Chem Commun (Camb). 2011; 47:4667–4669. [PubMed: 21409237]
17. Bogdanov AA Jr, Martin C, Weissleder R, Brady TJ. Trapping of dextran-coated colloids in liposomes by transient binding to aminophospholipid: preparation of ferrosomes. Biochim Biophys Acta. 1994; 1193:212–218. [PubMed: 7518693]
18. Bulte JW, Ma LD, Magin RL, Kamman RL, Hulstaert CE, Go KG, The TH, de Leij L. Selective MR imaging of labeled human peripheral blood mononuclear cells by liposome mediated incorporation of dextran-magnetite particles. Magn Reson Med. 1993; 29:32–37. [PubMed: 7678318]
19. Mulder WJ, Strijkers GJ, van Tilborg GA, Griffioen AW, Nicolay K. Lipid-based nanoparticles for contrast-enhanced MRI and molecular imaging. NMR Biomed. 2006; 19:142–164. [PubMed: 16450332]
20. van Zijl PC, Yadav NN. Chemical exchange saturation transfer (CEST): what is in a name and what isn't? Magn Reson Med. 2011; 65:927–948. [PubMed: 21337419]
21. Liu G, Song X, Chan KW, McMahon MT. Nuts and bolts of chemical exchange saturation transfer MRI. NMR Biomed. 2013; 26:810–828. [PubMed: 23303716]
22. Sherry AD, Woods M. Chemical exchange saturation transfer contrast agents for magnetic resonance imaging. Annu Rev Biomed Eng. 2008; 10:391–411. [PubMed: 18647117]
23. Terreno E, Castelli DD, Aime S. Encoding the frequency dependence in MRI contrast media: the emerging class of CEST agents. Contrast Media Mol Imaging. 2010; 5:78–98. [PubMed: 20419761]
24. Ward KM, Aletras AH, Balaban RS. A new class of contrast agents for MRI based on proton chemical exchange dependent saturation transfer (CEST). J Magn Reson. 2000; 143:79–87. [PubMed: 10698648]

25. McMahon MT, Gilad AA, DeLiso MA, Berman SM, Bulte JW, van Zijl PC. New "multicolor" polypeptide diamagnetic chemical exchange saturation transfer (DIACEST) contrast agents for MRI. Magn Reson Med. 2008; 60:803–812. [PubMed: 18816830]
26. Aime S, Delli Castelli D, Terreno E. Highly sensitive MRI chemical exchange saturation transfer agents using liposomes. Angew Chem Int Ed Engl. 2005; 44:5513–5515. [PubMed: 16052647]
27. Winter PM. Magnetic resonance chemical exchange saturation transfer imaging and nanotechnology. Wiley Interdiscip Rev Nanomed Nanobiotechnol. 2012; 4:389–398. [PubMed: 22422650]
28. Liu G, Moake M, Har-el YE, Long CM, Chan KW, Cardona A, Jamil M, Walczak P, Gilad AA, Sgouros G, van Zijl PC, Bulte JW, McMahon MT. In vivo multicolor molecular MR imaging using diamagnetic chemical exchange saturation transfer liposomes. Magn Reson Med. 2012; 67:1106–1113. [PubMed: 22392814]
29. Chan KW, Liu G, Song X, Kim H, Yu T, Arifin DR, Gilad AA, Hanes J, Walczak P, van Zijl PC, Bulte JW, McMahon MT. MRI-detectable pH nanosensors incorporated into hydrogels for in vivo sensing of transplanted-cell viability. Nat Mater. 2013; 12:268–275. [PubMed: 23353626]
30. Flament J, Geffroy F, Medina C, Robic C, Mayer JF, Meriaux S, Valette J, Robert P, Port M, Le Bihan D, Lethimonnier F, Boumezbeur F. In vivo CEST MR imaging of U87 mice brain tumor angiogenesis using targeted LipoCEST contrast agent at 7 T. Magn Reson Med. 2013; 69:179–187. [PubMed: 22378016]
31. Zhao JM, Har-el YE, McMahon MT, Zhou J, Sherry AD, Sgouros G, Bulte JW, van Zijl PC. Size-induced enhancement of chemical exchange saturation transfer (CEST) contrast in liposomes. J Am Chem Soc. 2008; 130:5178–5184. [PubMed: 18361490]
32. Kim M, Gillen J, Landman BA, Zhou J, van Zijl PC. Water saturation shift referencing (WASSR) for chemical exchange saturation transfer (CEST) experiments. Magn Reson Med. 2009; 61:1441–1450. [PubMed: 19358232]
33. Koch E, Pircher J, Czermak T, Gaitzsch E, Alig S, Mannell H, Niemeyer M, Krotz F, Wornle M. The endothelial tyrosine phosphatase SHP-1 plays an important role for vascular haemostasis in TNFalpha -induced inflammation in vivo. Mediators Inflamm. 2013; 2013:279781. [PubMed: 23766558]
34. McMahon MT, Gilad AA, Zhou J, Sun PZ, Bulte JW, van Zijl PC. Quantifying exchange rates in chemical exchange saturation transfer agents using the saturation time and saturation power dependencies of the magnetization transfer effect on the magnetic resonance imaging signal (QUEST and QUESP): Ph calibration for poly-L-lysine and a starburst dendrimer. Magn Reson Med. 2006; 55:836–847. [PubMed: 16506187]
35. Schiffelers RM, Ansari A, Xu J, Zhou Q, Tang Q, Storm G, Molema G, Lu PY, Scaria PV, Woodle MC. Cancer siRNA therapy by tumor selective delivery with ligand-targeted sterically stabilized nanoparticle. Nucleic Acids Res. 2004; 32:e149. [PubMed: 15520458]
36. Mulder WJ, Castermans K, van Beijnum JR, Oude Egbrink MG, Chin PT, Fayad ZA, Lowik CW, Kaijzel EL, Que I, Storm G, Strijkers GJ, Griffioen AW, Nicolay K. Molecular imaging of tumor angiogenesis using alphavbeta3-integrin targeted multimodal quantum dots. Angiogenesis. 2009; 12:17–24. [PubMed: 19067197]
37. Pekar J, Jezzard P, Roberts DA, Leigh JS Jr, Frank JA, McLaughlin AC. Perfusion imaging with compensation for asymmetric magnetization transfer effects. Magn Reson Med. 1996; 35:70–79. [PubMed: 8771024]
38. Hua J, Jones CK, Blakeley J, Smith SA, van Zijl PC, Zhou J. Quantitative description of the asymmetry in magnetization transfer effects around the water resonance in the human brain. Magn Reson Med. 2007; 58:786–793. [PubMed: 17899597]
39. Ling W, Regatte RR, Navon G, Jerschow A. Assessment of glycosaminoglycan concentration in vivo by chemical exchange-dependent saturation transfer (gagCEST). Proc Natl Acad Sci U S A. 2008; 105:2266–2270. [PubMed: 18268341]
40. Jones CK, Huang A, Xu JD, Edden RAE, Schar M, Hua J, Oskolkov N, Zaca D, Zhou JY, McMahon MT, Pillai JJ, van Zijl PCM. Nuclear Overhauser enhancement (NOE) imaging in the human brain at 7 T. Neuroimage. 2013; 77:114–124. [PubMed: 23567889]

41. Cai K, Haris M, Singh A, Kogan F, Greenberg JH, Hariharan H, Detre JA, Reddy R. Magnetic resonance imaging of glutamate. Nat Med. 2012; 18:302–306. [PubMed: 22270722]
42. Haris M, Nanga RP, Singh A, Cai K, Kogan F, Hariharan H, Reddy R. Exchange rates of creatine kinase metabolites: feasibility of imaging creatine by chemical exchange saturation transfer MRI. NMR Biomed. 2012; 25:1305–1309. [PubMed: 22431193]
43. Haris M, Singh A, Cai K, Nath K, Crescenzi R, Kogan F, Hariharan H, Reddy R. MICEST: a potential tool for non-invasive detection of molecular changes in Alzheimer's disease. J Neurosci Methods. 2013; 212:87–93. [PubMed: 23041110]
44. Jin T, Autio J, Obata T, Kim SG. Spin-locking versus chemical exchange saturation transfer MRI for investigating chemical exchange process between water and labile metabolite protons. Magn Reson Med. 2011; 65:1448–1460. [PubMed: 21500270]
45. Chan KW, McMahon MT, Kato Y, Liu G, Bulte JW, Bhujwalla ZM, Artemov D, van Zijl PC. Natural D-glucose as a biodegradable MRI contrast agent for detecting cancer. Magn Reson Med. 2012; 68:1764–1773. [PubMed: 23074027]
46. Nasrallah FA, Pages G, Kuchel PW, Golay X, Chuang KH. Imaging brain deoxyglucose uptake and metabolism by glucoCEST MRI. J Cereb Blood Flow Metab. 2013; 33:1270–1278. [PubMed: 23673434]
47. Walker-Samuel S, Ramasawmy R, Torrealdea F, Rega M, Rajkumar V, Johnson SP, Richardson S, Goncalves M, Parkes HG, Arstad E, Thomas DL, Pedley RB, Lythgoe MF, Golay X. In vivo imaging of glucose uptake and metabolism in tumors. Nat Med. 2013; 19:1067–1072. [PubMed: 23832090]
48. Lopez-Munoz F, Ucha-Udabe R, Alamo C. The history of barbiturates a century after their clinical introduction. Neuropsychiatr Dis Treat. 2005; 1:329–343. [PubMed: 18568113]
49. Tateoka Y, Kimura T, Yamazaki F, Watanabe K, Yamamoto I. Central depressant effect of barbituric acid and N,5,5-triallylbarbituric acid in mice. Yakugaku Zasshi. 1986; 106:504–510. [PubMed: 3761160]
50. Maffii G, Silvestrini B, Bianchi G. Pharmacological activity of beta-lactams. II. Systemic effects of 3-methyl-3-phenyl-2-azetidinone and of 3-ethyl-3-phenyl-2-azetidinone. Farmaco Sci. 1959; 14:269–287. [PubMed: 13653108]
51. Bulte JW, de Cuyper M, Despres D, Frank JA. Short- vs. long-circulating magnetoliposomes as bone marrow-seeking MR contrast agents. J Magn Reson Imaging. 1999; 9:329–335. [PubMed: 10077033]
52. Caride VJ, Sostman HD, Winchell RJ, Gore JC. Relaxation enhancement using liposomes carrying paramagnetic species. Magn Reson Imaging. 1984; 2:107–112. [PubMed: 6530919]
53. Kabalka G, Buonocore E, Hubner K, Moss T, Norley N, Huang L. Gadolinium-labeled liposomes: targeted MR contrast agents for the liver and spleen. Radiology. 1987; 163:255–258. [PubMed: 3454163]
54. Zucker D, Marcus D, Barenholz Y, Goldblum A. Liposome drugs' loading efficiency: a working model based on loading conditions and drug's physicochemical properties. J Control Release. 2009; 139:73–80. [PubMed: 19508880]
55. Jones CK, Polders D, Hua J, Zhu H, Hoogduin HJ, Zhou J, Luijten P, van Zijl PC. In vivo three-dimensional whole-brain pulsed steady-state chemical exchange saturation transfer at 7 T. Magn Reson Med. 2012; 67:1579–1589. [PubMed: 22083645]
56. Dixon WT, Hancu I, Ratnakar SJ, Sherry AD, Lenkinski RE, Alsop DC. A multislice gradient echo pulse sequence for CEST imaging. Magn Reson Med. 2010; 63:253–256. [PubMed: 19918889]
57. Scheidegger R, Vinogradov E, Alsop DC. Amide proton transfer imaging with improved robustness to magnetic field inhomogeneity and magnetization transfer asymmetry using saturation with frequency alternating RF irradiation. Magn Reson Med. 2011; 66:1275–1285. [PubMed: 21608029]
58. Zu Z, Janve VA, Xu J, Does MD, Gore JC, Gochberg DF. A new method for detecting exchanging amide protons using chemical exchange rotation transfer. Magn Reson Med. 2013; 69:637–647. [PubMed: 22505325]

59. Yadav NN, Jones CK, Xu J, Bar-Shir A, Gilad AA, McMahon MT, van Zijl PC. Detection of rapidly exchanging compounds using on-resonance frequency-labeled exchange (FLEX) transfer. Magn Reson Med. 2012; 68:1048–1055. [PubMed: 22837066]

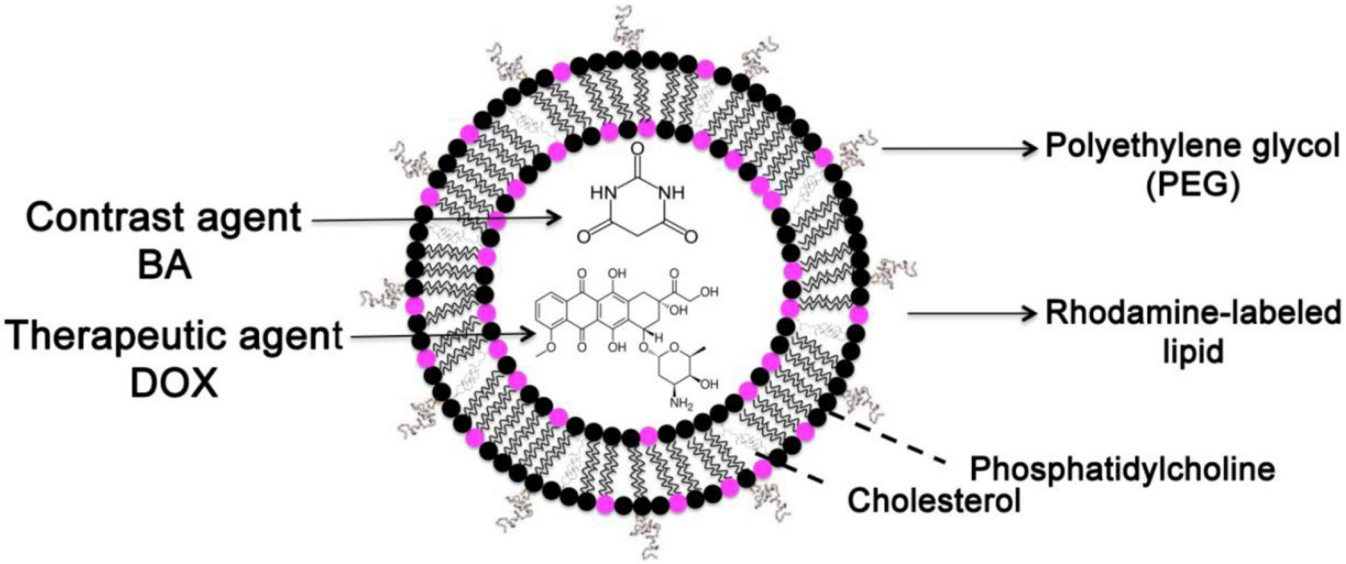

Fig. 1.
Cartoon depicting BA/DOX co-loaded diaCEST liposome.

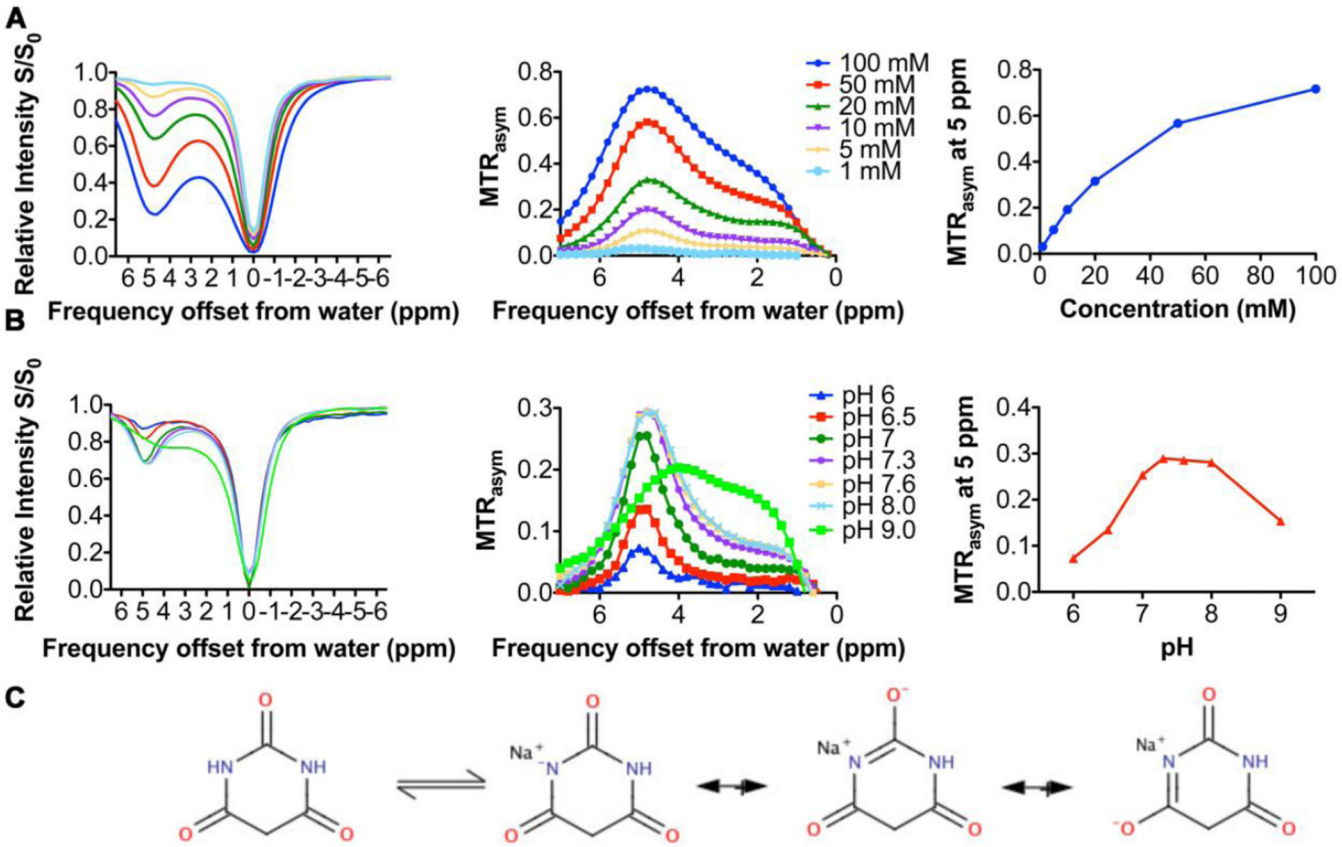

Fig. 2.

CEST properties of BA and its dependence on concentration and pH. **(A–B)** CEST contrast of BA in solution at different **(A)** concentrations and **(B)** pH values at 37°C. **(C)** Structure of keto-enol tautomerism of BA and its acid- or base-catalyzed forms.

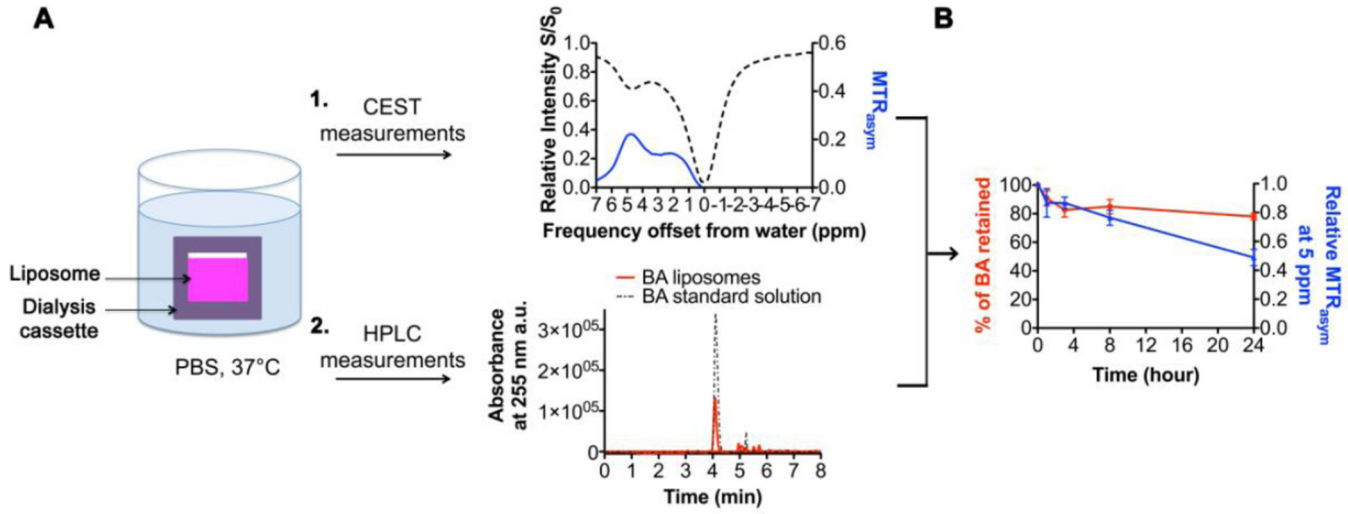

Fig. 3.

CEST contrast stability and retention of BA in diaCEST liposomes *in vitro*. **(A)** Cartoon depicting the method for studying the BA stability of the optimized formulation of diaCEST liposomes. Liposomes were dialyzed against PBS at 37°C and two separate measurements were performed: 1) CEST contrast was measured at specific time points and 2) the amount of BA remaining within the liposomes was determined using HPLC. **(B)** Profiles of the CEST contrast and amount of BA retained as a function of dialysis time of diaCEST liposomes. Values were normalized based on the initial intensity/dose at 0 h. Data represent mean ± S.D. (n=3).

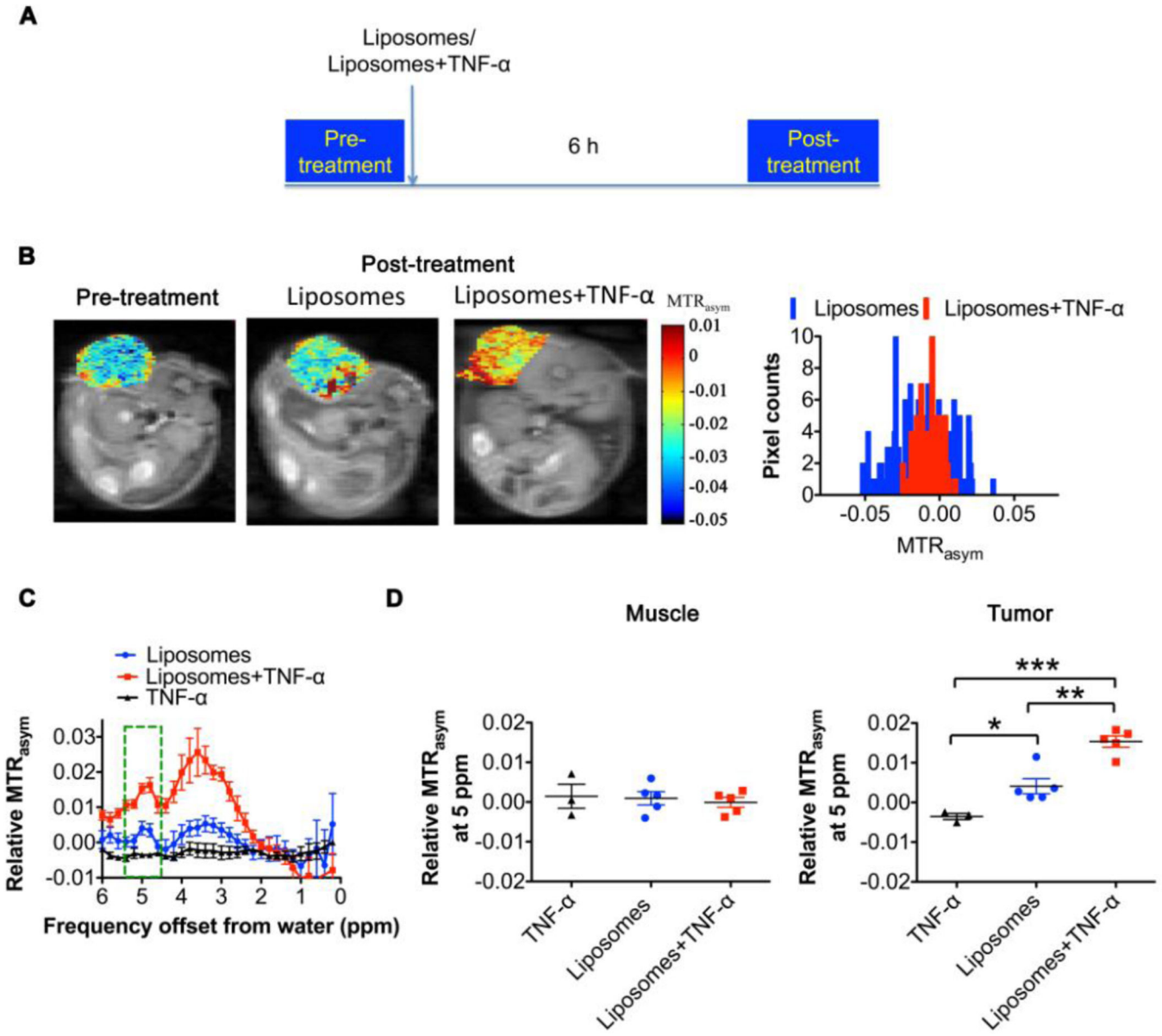

Fig. 4.

In vivo CEST imaging of diaCEST liposomes injected i.v. in mice bearing CT26 subcutaneous tumors. **(A)** Time line of the i.v. injection of liposomes and/or TNF-α as well as the pre-treatment and post-treatment CEST imaging before and 6 hours after the injection, respectively. **(B)** MTR_{asym} maps at 5 ppm for representative animals before and after treatment. Corresponding MTR_{asym} histogram analysis is shown in the right panel. Relative MTR_{asym} profiles (post-treatment – pre-treatment) for the **(C)** Entire tumor regions in the Liposome group (n=5), the Liposomes+TNF-α group (n=5), and the control group with TNF-α injection only (n=3), with the unique peak of BA CEST contrast at 5 ppm highlighted by a green box. **(D)** Left panel shows the relative MTR_{asym} at 5 ppm for muscle for the three groups; right panel shows the entire tumor for the three groups. (*, $P<0.05$; **, $P<0.01$; ***, $P<0.001$, one-way ANOVA).

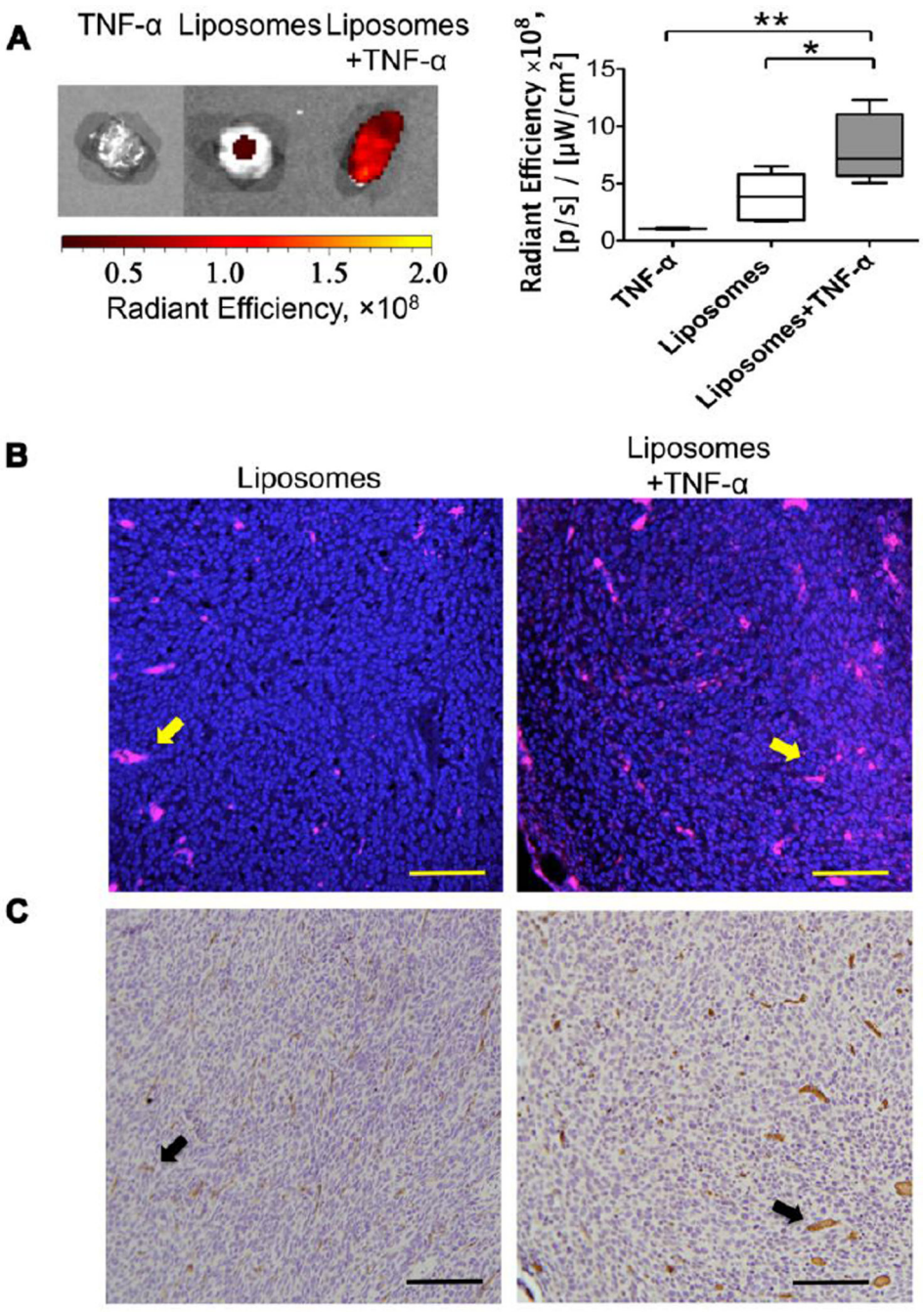

Fig. 5.

Validation of the diaCEST approach using fluorescence imaging and histology. **(A)** Representative fluorescence images and average fluorescence intensity (measured as radiant efficiency) of tumors harvested from the TNF-α control group (n=3), the Liposome group (n=5) and the Liposome+TNF-α group (n=5). (*, $P<0.05$; **, $P<0.01$, one-way ANOVA). **(B)** Fluorescence histology of excised tumors showing the relative accumulation and distribution of rhodamine-labeled diaCEST liposomes (red, yellow arrows) for the Liposome group and the Liposome+TNF-α group. Nuclei are stained with DAPI (blue). **(C)** CD31

staining shows distribution of blood vessels (black arrows) in sections of similar regions in (B). Arrows indicate representative regions (Scale bar=100 μm).

Table 1

Physicochemical properties of the different diaCEST liposome formulations

Formulation	Size (nm)		PDI		BA:lipid	DOX:lipid	CEST contrast
	at 0h	at 24h	at 0h	at 24h	ratio (%)	ratio (%)	at 5 ppm (%)
EggPC	133±6	155±1	0.14±0.04	0.10±0.00	22±8	0.9±0.6	19±1
SoyPC	171±7	177±1	0.09±0.02	0.09±0.00	19±3	1.5±0.2	20±3
DPPC	158±6	151±3	0.10±0.03	0.09±0.01	20±1	1.1±0.1	24±6
HSPC	178±4	174±3	0.11±0.05	0.05±0.02	22±1	1.2±0.1	23±1
DSPC	167±1	170±2	0.10±0.01	0.03±0.02	25±1	1.1±0.1	30±1

Data represent mean ± S.D. (n≥3).